Spectrally Consistent Scattering, Absorption, and Polarization Properties of Atmospheric Ice Crystals at Wavelengths from 0.2 to 100 μm

PING YANG,* LEI BI,* BRYAN A. BAUM,[+] KUO-NAN LIOU,[#] GEORGE W. KATTAWAR,[@] MICHAEL I. MISHCHENKO,[&] AND BENJAMIN COLE*

*Department of Atmospheric Sciences, Texas A&M University, College Station, Texas
[+] Space Science and Engineering Center, University of Wisconsin—Madison, Madison, Wisconsin
[#] Joint Institute for Earth System Science and Engineering, and Department of Atmospheric and Oceanic Sciences, University of California, Los Angeles, Los Angeles, California
[@] Department of Physics and Astronomy, Texas A&M University, College Station, Texas
[&] NASA Goddard Institute for Space Studies, New York, New York

(Manuscript received 7 February 2012, in final form 14 June 2012)

ABSTRACT

A data library is developed containing the scattering, absorption, and polarization properties of ice particles in the spectral range from 0.2 to 100 μm. The properties are computed based on a combination of the Amsterdam discrete dipole approximation (ADDA), the T-matrix method, and the improved geometric optics method (IGOM). The electromagnetic edge effect is incorporated into the extinction and absorption efficiencies computed from the IGOM. A full set of single-scattering properties is provided by considering three-dimensional random orientations for 11 ice crystal habits: droxtals, prolate spheroids, oblate spheroids, solid and hollow columns, compact aggregates composed of eight solid columns, hexagonal plates, small spatial aggregates composed of 5 plates, large spatial aggregates composed of 10 plates, and solid and hollow bullet rosettes. The maximum dimension of each habit ranges from 2 to 10 000 μm in 189 discrete sizes. For each ice crystal habit, three surface roughness conditions (i.e., smooth, moderately roughened, and severely roughened) are considered to account for the surface texture of large particles in the IGOM applicable domain. The data library contains the extinction efficiency, single-scattering albedo, asymmetry parameter, six independent nonzero elements of the phase matrix (P_{11}, P_{12}, P_{22}, P_{33}, P_{43}, and P_{44}), particle projected area, and particle volume to provide the basic single-scattering properties for remote sensing applications and radiative transfer simulations involving ice clouds. Furthermore, a comparison of satellite observations and theoretical simulations for the polarization characteristics of ice clouds demonstrates that ice cloud optical models assuming severely roughened ice crystals significantly outperform their counterparts assuming smooth ice crystals.

1. Introduction

Numerous studies have elaborated on the important role that natural ice clouds and contrails play in the atmospheric radiation budget essential to weather and climate systems [see Liou (1986); Lynch et al. (2002); Baran (2009); Yang et al. (2010); and references therein]. The single-scattering properties of ice crystals are fundamental to the development of a variety of applications involving these clouds. For example, the properties are indispensable in both the computation and parameterization of the bulk broadband radiative properties of ice clouds (Fu et al. 1998; McFarquhar et al. 2002; Key et al. 2002; Gu et al. 2003; Edwards et al. 2007; Liou et al. 2008), in radiative transfer simulations (Mayer and Kylling 2005), and in assessing the radiative forcing of ice clouds (Wendisch et al. 2007; Edwards et al. 2007). For operational retrievals, the single-scattering properties are averaged over various particle size distributions with an assumed habit prescription (Baum et al. 2005, 2011; Yue et al. 2007; Baran 2009). The resulting bulk-scattering properties are used in radiative transfer models to simulate the reflectance and transmittance associated with ice clouds over a range of conditions, and are tabulated in lookup tables (LUTs) for use in

Corresponding author address: Prof. Ping Yang, Department of Atmospheric Sciences, Texas A&M University, TAMU-3150, College Station, TX 77843.
E-mail: pyang@tamu.edu

DOI: 10.1175/JAS-D-12-039.1

subsequent data reduction to infer ice cloud optical thickness and effective particle size from airborne or satellite observations (Platnick et al. 2003; King et al. 2004; Huang et al. 2004; Wang et al. 2009; Minnis et al. 2011). The need for consistency in the optical properties over a wide spectral range becomes evident when comparing retrievals from sensors taking measurements with quite different methods such as solar wavelength techniques, polarization techniques, or infrared wavelength techniques (e.g., Baran and Francis 2004; Ham et al. 2009; Zhang et al. 2009).

The single-scattering properties for individual ice habits have been reported in numerous articles by Wendling et al. (1979), Cai and Liou (1982), Takano and Liou (1989, 1995), Muinonen (1989), Macke (1993), Macke et al. (1996b), Yang and Liou (1996a,b), Sun et al. (1999), Havemann and Baran (2001), Baran et al. (2001), Borovoi et al. (2002), Hesse and Ulanowski (2003), Um and McFarquhar (2007), and Nakajima et al. (2009). Moreover, several previous studies have developed ice particle single-scattering properties in relatively limited domains. For example, using a ray-tracing model developed by Wendling et al. (1979) with some enhancements, Hess and Wiegner (1994) and Hess et al. (1998) created a single-scattering property database for hexagonal ice columns and plates at 12 wavelengths from the ultraviolet (UV) to the infrared (IR) spectral region. Yang et al. (2000) developed the single-scattering properties in the solar spectrum from 0.2 to 5 μm for six ice particle habits: plates, columns, hollow columns, planar bullet rosettes with four branches, three-dimensional (3D) bullet rosettes with six branches, and compact aggregates of solid columns. Yang et al. (2005) published a database for droxtals, plates, columns, hollow columns, 3D bullet rosettes, and compact aggregates of columns at 49 discrete wavelengths between 3 and 100 μm. The single-scattering properties were calculated by a combination of two scattering computational models: the finite-difference time domain method (FDTD) (Yee 1966; Yang and Liou 1996a; Sun et al. 1999) and the improved geometric optics method (IGOM) (Yang and Liou 1996b).

The data libraries presented by Yang et al. (2000, 2005) contained several inconsistencies in the solar and thermal IR spectral regions because of differences in the particle shapes and the computational methodologies used in the computations. An empirical approach known as the composite method (Fu et al. 1998), which partially uses the concept of "equivalent" spheres for nonspherical particles, was employed to merge the extinction and absorption efficiencies in the size parameter region of overlapping FDTD and IGOM results in the IR database (Yang et al. 2005). The inconsistencies were also generated from different discretizations of the particle size bins employed in the solar and IR regions and from slightly different particle aspect ratios for some habits. Additionally, in Yang et al. (2000), the intensity (P_{11} component) contained an artificial term referred to as the delta transmission (Takano and Liou 1989; Mishchenko and Macke 1998), which resulted from either the conventional geometric optics method (Cai and Liou 1982; Takano and Liou 1989) or a simplification in the IGOM related to the treatment of the forward peak in the phase function for large particles. The delta transmission term produced complications in radiative transfer simulations as well as in the interpretation of the effective optical thickness of ice clouds.

This study is intended to develop a spectrally consistent data library containing the scattering, absorption, and polarization properties of a set of 11 randomly oriented ice crystal habits at wavelengths from 0.2 to 100 μm. The maximum diameters for each habit range from 2 to 10 000 μm. The ice particle habits include quasi-spherical particles (droxtals, prolate spheroids, and oblate spheroids), hexagonal plates, solid and hollow hexagonal columns, small and large spatial aggregates of plates defined following Xie et al. (2011), compact aggregates of solid columns, and solid and hollow 3D bullet rosettes (Yang et al. 2008a). The data library provides information relating to the volume and projected area of each habit as well as the asymmetry parameter, single-scattering albedo, extinction and absorption cross sections/efficiencies, and the six nonzero elements of the phase matrix.

The new data library presented in this paper provides the basic and consistent single-scattering data for a selection of ice crystal sizes and shapes observed in the atmosphere. The library adds to previous work regarding the derivation of ice particle optical properties in the following four ways: 1) the scattering models used to solve for the various ice particle optical properties have been improved (e.g., Yang et al. 2008a; Yang and Liou 2009a,b; Bi et al. 2008, 2011a,b; Liou et al. 2010, 2011) since the publication of the previous databases (Yang et al. 2000, 2005), and, at the same time, the unphysical delta-transmission feature has been removed by means of a new approach (Bi et al. 2008); 2) the calculations employ the real and imaginary indices of refraction for ice presented by Warren and Brandt (2008) to conduct the necessary single-scattering and polarization calculations; 3) the aspect ratios used in the calculations are consistent for a spectral range from 0.2 to 100 μm; and 4) the composite method (Fu et al. 1998) was not adopted to merge the scattering properties at size parameters when the Amsterdam discrete dipole

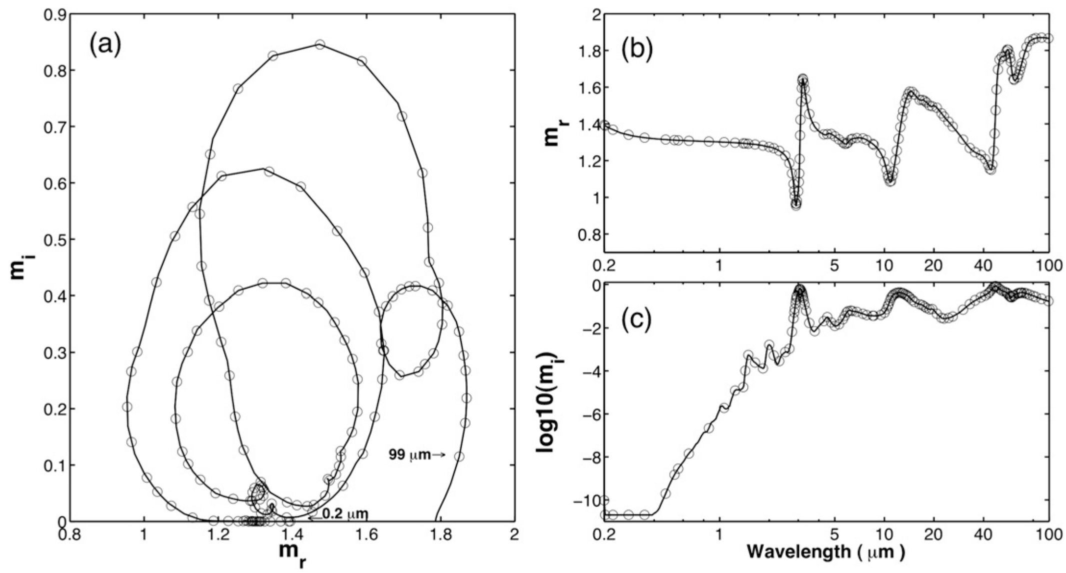

FIG. 1. (a) Correlation of the real and imaginary part of the refractive index. (b) Real part of the refractive index. (c) Imaginary part of the refractive index.

approximation (ADDA) and IGOM solutions overlap, but a new approach was developed that includes the edge effect for the extinction efficiency and the above-/below-edge effect for the absorption efficiency (Nussenzveig and Wiscombe 1980; Baran and Havemann 1999) in the IGOM solutions. With the new approach, the results for the extinction and absorption efficiencies are continuous as functions of the size parameter x proportional to the ratio of the particle circumference to the incident wavelength, regardless of whether the properties are computed from the ADDA or IGOM. In this study, the T-matrix method (Mishchenko et al. 1996) was used for prolate and oblate spheroids that may approximate the shapes of small ice crystals in aircraft contrails (Mishchenko and Sassen 1998; Iwabuchi et al. 2012). While quasi-spherical particles are sometimes observed in images from cloud probes, perhaps owing to insufficient optical resolution, the underlying ice crystal morphology can be more complex (Connolly et al. 2007). Calculations for other faceted habits are performed using the ADDA computational program (Yurkin et al. 2007b; http://code.google.com/p/a-dda/downloads/list) for $x \le 20$ and an improved and refined version of the IGOM (Bi et al. 2009) for $x > 20$. Because no single model among the existing electromagnetic scattering computational methods (Mishchenko et al. 2000; Kahnert 2003; Wriedt 2009) can be employed over the entire range of size parameters and habits, significant effort was required to merge the ADDA and IGOM solutions as seamlessly as possible.

The paper is organized as follows: section 2 explains the methodology for the development of the single-scattering data library, section 3 illustrates the single-scattering properties of a number of ice crystal habits, and section 4 summarizes the present work.

2. Methodology

In our calculations, we used the most recent compilation of the refractive index of ice (Warren and Brandt 2008) from 0.2 to 100 μm. Figure 1a shows the imaginary part of the ice refractive index m_i versus the corresponding real part m_r, while Figs. 1b and 1c, respectively, show the variations of m_i and m_r as functions of wavelength. In Fig. 1a, the open circle symbols signify the 445 spectral points chosen for the detailed scattering computations. As illustrated in Figs. 1b and 1c, the spectral points for the refractive index were selected at the maxima and minima of either m_i or m_r. Extensive sensitivity studies, using spheres, were performed to ensure that the optical properties at wavelengths not coinciding with the selected spectral points could be obtained via interpolation and with negligible errors by using the properties at two nearby spectral points.

The left and right panels in Fig. 2 respectively show the grid points selected for particle size and wavelength in the computational domain of the previous datasets (Yang et al. 2000, 2005) and the present library. As shown in the left panel, fewer particle size bins were selected in the solar spectral region (Yang et al. 2000) than in the IR spectral region (Yang et al. 2005). This inconsistency is circumvented by the present selection of particle sizes shown in the right panel of Fig. 2. In this

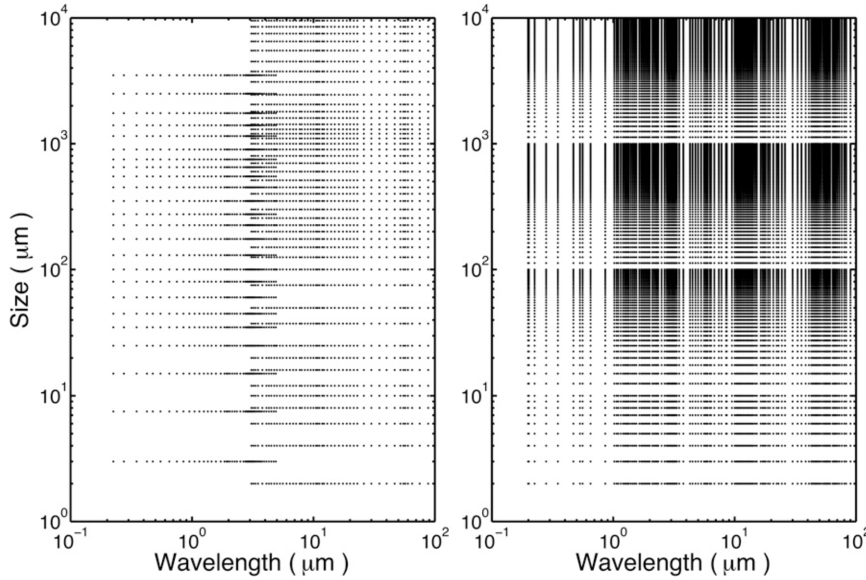

FIG. 2. Grid points in the computational domain of the particle size and the wavelength. (left) The previous databases. (right) The present database.

study, 189 points are selected for particle sizes ranging from 2 to 10 000 μm, whereas only 24 sizes between 3 and 3500 μm were used in Yang et al. (2000) and only 45 sizes between 2 and 10 000 μm were used in Yang et al. (2005).

In situ measurements have indicated ice crystals to have predominantly hollow structures (Walden et al. 2003; Schmitt and Heymsfield 2007), which affected the choice of ice crystal habits considered in this study and shown in Fig. 3. The first row shows quasi-spherical ice crystals (droxtal, prolate spheroid, and oblate spheroid), the second row shows solid and hollow hexagonal columns and compact aggregates of hexagonal columns, the third row shows hexagonal plates and spatial aggregates of hexagonal plates, and the fourth row shows solid and hollow bullet rosettes. In addition to the variety of habits shown in Fig. 3, the effect of surface roughness is considered in the current IGOM calculations. As a proxy to mimic particle surface roughness, the surface slope is distorted randomly for each incident ray. Similar to the approach suggested by Cox and Munk (1954) for defining the roughness conditions of the sea surface, a normal distribution of the surface slope for a particle's surface is defined by

$$P(Z_x, Z_y) = \frac{1}{\sigma^2 \pi} \exp\left(-\frac{Z_x^2 + Z_y^2}{\sigma^2}\right), \tag{1}$$

where Z_x and Z_y indicate the local slope variations of the particle's surface along two orthogonal directions (i.e., the x and y directions). The parameter σ is associated with the degree of surface roughness with larger values of σ denoting rougher particle surfaces. In the present simulations, three values for σ are chosen: $\sigma = 0$ (smooth surface), $\sigma = 0.03$ (moderate surface roughness), and $\sigma = 0.5$ (severe surface roughness). Yang and Liou (1998) provide a more complete description of the surface slopes incorporated into the IGOM.

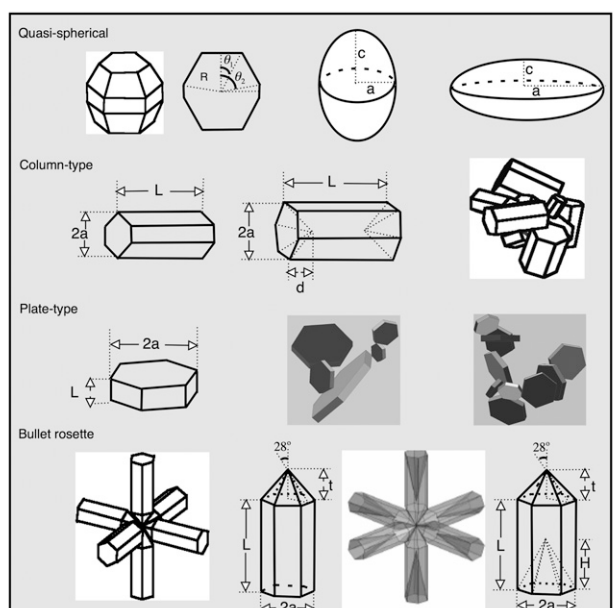

FIG. 3. Ice crystal habits: quasi-spherical, column-type, plate-type, and bullet rosette particles.

TABLE 1. Geometric parameters of ice crystal habits.

Habit	No.	a	L	α	β	γ	X_0	Y_0	Z_0
Droxtal	$\theta_1 = 32.35°, \theta_2 = 71.81°$								
Prolate spheroids	$a/c = 0.725, 0.5, 0.25$								
Oblate spheroids	$a/c = 1.25, 2.5, 4$								
Column	$2a/L = \begin{cases} 0.7, & L < 100\,\mu\text{m} \\ 6.96/\sqrt{L}, & L \geq 100\,\mu\text{m} \end{cases}$								
Hollow column	$2a/L = \begin{cases} 0.7, & L < 100\,\mu\text{m} \\ 6.96/\sqrt{L}, & L \geq 100\,\mu\text{m} \end{cases}, d = 0.25L$								
Aggregate of 8 columns	No.	a	L	α	β	γ	X_0	Y_0	Z_0
	1	46	158	23	50	−54	0	0	0
	2	40	124	16	81	156	15.808	105.189	−60.108
	3	28	78	5	57	94	−26.691	73.005	47.369
	4	48	126	13	76	130	−85.688	−39.19	−11.643
	5	53	144	11	29	−21	104.532	33.08	27.801
	6	19	54	8	62	−164	35.923	−49.692	−37.533
	7	34	102	29	41	60	40.11	−57.227	110.238
	8	43	138	19	23	−122	−9.7524	−129.313	57.131
Plate	$2a/L = \begin{cases} 1, & a \leq 2\,\mu\text{m} \\ 0.2914a + 0.4172, & 2 < a < 5\,\mu\text{m} \\ 0.8038a^{0.526}, & a \geq 5\,\mu\text{m} \end{cases}$								
Aggregate of 5 plates	No.	a	L	α	β	γ	X_0	Y_0	Z_0
	1	24	11.223	0	0	0	0	0	0
	2	27	11.868	−82.655	175.767	−78.103	−5.664	43.934	−13.203
	3	22	10.770	−7.651	−23.688	−132.443	−13.519	21.792	−25.347
	4	20	10.294	−101.85	155.069	−50.708	18.656	68.178	−29.741
	5	38	13.955	−118.412	−30.374	−42.438	−3.161	71.109	−54.738
Aggregate of 10 plates	No.	a	L	α	β	γ	X_0	Y_0	Z_0
	1	77	19.503	0	0	0	0	0	0
	2	58	17.052	−177.37	64.830	−27.941	99.193	4.561	−7.3748
	3	75	19.261	−146.82	242.688	−69.303	115.667	8.322	−105.096
	4	42	14.633	99.056	53.002	77.723	90.671	21.580	−175.875
	5	47	15.434	13.853	224.545	33.875	−18.069	47.826	47.2620
	6	72	18.892	−167.855	43.472	−23.762	97.754	−22.864	−249.469
	7	45	15.119	−108.623	217.569	−15.595	7.019	−35.116	−189.123
	8	65	17.998	−51.308	−72.4	−173.509	−14.105	−132.186	−184.875
	9	74	19.139	−87.353	75.060	−49.382	32.361	−171.149	−155.846
	10	70	18.6414	−98.0649	−111.24	25.5653	50.0817	−228.132	−81.978
Solid bullet rosettes	$2a/L = 2.3104L^{-0.37}$, $t = (\sqrt{3}/2)a/\tan(28°)$								
Hollow bullet rosettes	$2a/L = 2.3104L^{-0.37}$, $t = (\sqrt{3}/2)a/\tan(28°)$, $H = 0.5(t + L)$								

Table 1 provides the aspect ratios of the ice crystal habits shown in Fig. 3. In the case of an aggregate of columns or plates, the semiwidth a and length L of each hexagonal element of the aggregate are on a relative scale, the center of the element in the particle system is denoted by three coordinates (X_0, Y_0, Z_0), and the orientation of the element is specified in terms of three Euler angles (α, β, γ) with Z–Y–Z rotations. For columns, plates, and droxtals, the aspect ratios used are from the literature (Arnott et al. 1994; Auer and Veal 1970; Mitchell and Arnott 1994; Pruppacher and Klett 1980; Yang et al. 2003; Zhang et al. 2004) and are similar to those used by Yang et al. (2000, 2005). The geometries of solid and hollow bullet rosettes used are the same as those defined in Yang et al. (2000, 2008a). With the aspect ratio relationship defined in Table 1 for a solid or hollow bullet rosette with a given maximum dimension D, the length of the columnar portion of a bullet branch can be obtained by solving the following nonlinear equation:

$$4L^2 + 15.0532L^{1.63} + 19.4987L^{1.26} = D^2. \qquad (2)$$

As in Yang et al. (2000, 2005), ice crystals are assumed to be randomly oriented in space with an equal number of mirror positions. In this case, the 4×4 phase matrix has six independent elements (van de Hulst 1957; Bohren and Huffman 1983; Liou 2002; Mishchenko et al. 2002). Specifically, the incident and scattered Stokes parameters, (I_i, Q_i, U_i, V_i) and (I_s, Q_s, U_s, V_s), are related as follows:

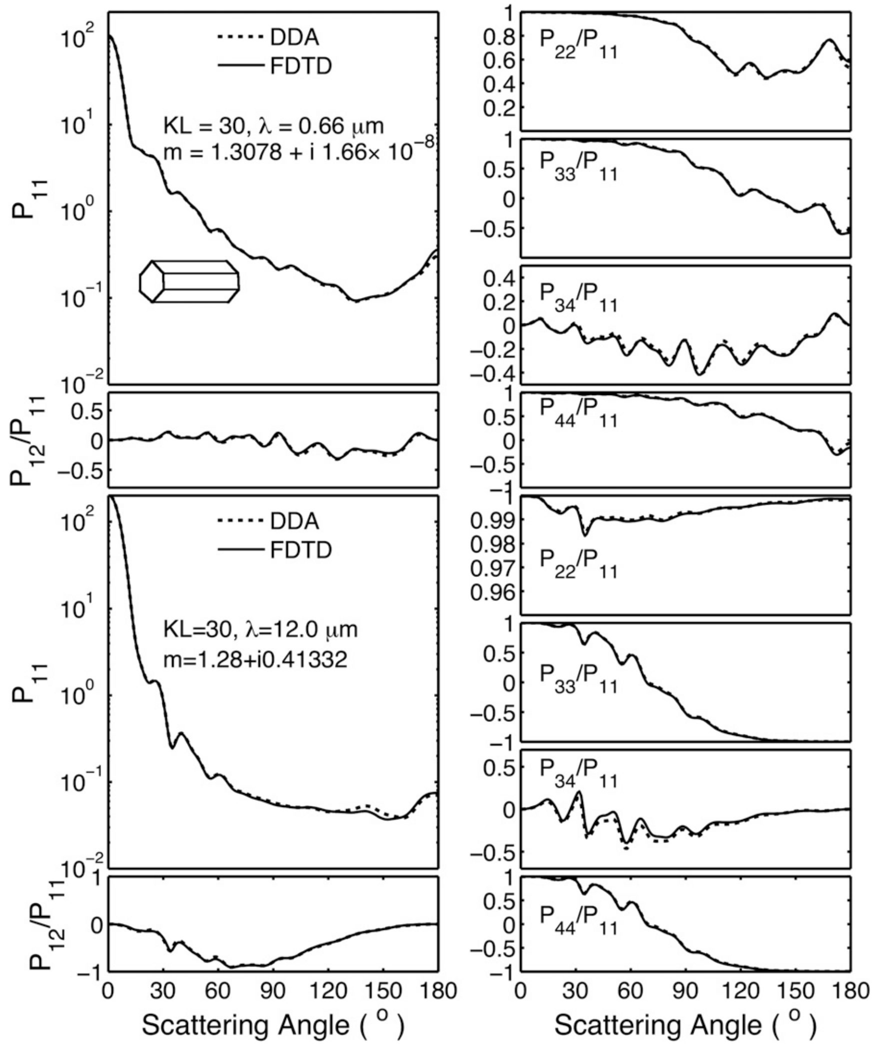

FIG. 4. Comparison of the phase matrix elements from the FDTD and the ADDA at the wavelengths of 0.66 and 12 μm.

$$\begin{bmatrix} I_s \\ Q_s \\ U_s \\ V_s \end{bmatrix} = \frac{\sigma_s}{4\pi r^2} \begin{bmatrix} P_{11} & P_{12} & 0 & 0 \\ P_{12} & P_{22} & 0 & 0 \\ 0 & 0 & P_{33} & P_{34} \\ 0 & 0 & -P_{34} & P_{44} \end{bmatrix} \begin{bmatrix} I_i \\ Q_i \\ U_i \\ V_i \end{bmatrix}, \quad (3)$$

where σ_s is the scattering cross section and r is the distance between the scattering particle and the point of observation. In the current data library, all the nonzero phase matrix elements in Eq. (3) are included and the phase matrix is a function of the scattering angle and invariant with the azimuthal angle.

In Yang et al. (2005), the FDTD method was applied to small size parameters ($x \leq 20$); however, we have used the ADDA for application to this size parameter range. The FDTD is based on the time-dependent Maxwell equations, whereas the ADDA solves the electromagnetic scattering problem involving a dielectric particle in the frequency domain. Although the FDTD and ADDA differ substantially from a computational perspective, their numerical solutions are consistent. As an example, Fig. 4 shows the nonzero phase matrix elements of randomly oriented hexagonal columns at two wavelengths: 0.66 and 12 μm. The orientation of the particle is specified through Euler angles (α, β, γ) in the common Z–Y–Z convention. In Fig. 4, the phase matrix is averaged using 128 α angles, 17 β angles, and 3 γ angles. For each FDTD and ADDA simulation (51 total in terms of the β and γ dependence), the phase matrix is averaged through 128 scattering planes. Excellent agreement between the FDTD solution and its ADDA counterpart is clearly shown in the figure. Yurkin et al. (2007a) investigated the computational efficiency of the FDTD and ADDA techniques for nonabsorbing particles and found the ADDA to be more efficient than the FDTD when the refractive index is smaller than 1.4; however, the opposite was found for larger values of the refractive index. Because the FDTD and ADDA yield the same numerical results for the spectrum considered in this study, the choice between the two methods is primarily a matter of computational time. The ADDA method is used for small size parameters regardless of the value of the refractive index at a selected wavelength.

In the ADDA simulations, the number of dipoles per wavelength (labeled ''dpl'' in the software) is a critical computational parameter that controls numerical accuracy. Two criteria were used to set up this parameter: (i) dpl $>10\,|m|$, where m is the refractive index, and (ii) the dpl should be sufficiently large to approximately represent particle geometry. For complex particle geometries, criterion (i) is insufficient for representing particle geometry through dipoles and may cause shape errors. The number of orientations is another parameter that impacts the accuracy of orientation-averaged single-scattering properties. The ADDA employs the Romberg integration technique (Davis and Rabinowitz 1975) to perform the orientation average with a prescribed accuracy. Figure 5 shows the number of orientations specified in the ADDA simulations for solid hexagonal columns at four representative wavelengths with a prescribed accuracy of 10^{-5}. The number of ADDA simulations depends on the number of discretized angles of β and γ, and the sixfold rotational symmetry was taken into account in setting up γ. The number of orientations generally increases with the size parameter. A large number of orientations increases the computational load of the ADDA method and is a limiting factor, although the ADDA method can handle a moderate size parameter for a single orientation.

We use the IGOM to perform the computations for the size parameter range beyond the modeling capabilities of the ADDA. As compared with the IGOM code used in Yang et al. (2005), some improvements are incorporated in the present algorithm. We employ 1) a more efficient recursive ray-tracing algorithm (Bi et al. 2011b) instead of the Monte Carlo ray tracing described in Yang and Liou (1998), 2) an improved near-to-far-field mapping algorithm (Bi et al. 2009), and 3) an improved approach to account for the external reflection of randomly oriented particles to reduce noise near the backscattering angle (Bi et al. 2011a). For example, for convex faceted particles (column, plate, and droxtal), the algorithm described in Bi et al. (2011b) is used to compute the single-scattering properties for moderate size parameters.

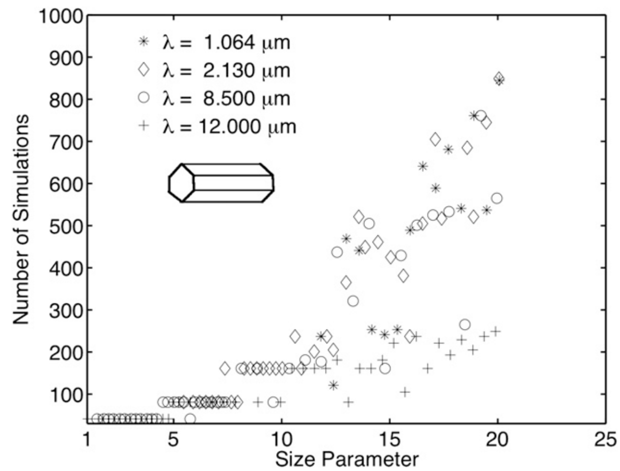

FIG. 5. Number of ADDA simulations (or particle orientations specified by β and γ) at four representative wavelengths in the hexagonal columns case.

Yang et al. (2005) used a composite method (Fu et al. 1998) based on a weighted combination of the Lorenz–Mie and IGOM solutions to improve the accuracy of the extinction and absorption efficiencies at moderate to large size parameters. In this study, a physically rational approach is employed to include the edge effect on the extinction efficiency and the above-/below-edge effect on the absorption efficiency (van de Hulst 1957; Nussenzveig and Wiscombe 1980; Liou et al. 2010). To briefly describe the edge effect, we consider the case of light scattering by a sphere in the framework of the localization principle following van de Hulst (1957). With the use of the standard notations for the Lorenz–Mie solution (Bohren and Huffman 1983; Liou 2002; Mishchenko et al. 2002), the nonzero elements of the amplitude scattering matrix associated with a sphere can be written in the form

$$S_1 = \sum_{n=1}^{\infty} \frac{2n+1}{n(n+1)}(a_n\pi_n + b_n\tau_n) \quad \text{and} \tag{4}$$

$$S_2 = \sum_{n=1}^{\infty} \frac{2n+1}{n(n+1)}(a_n\tau_n + b_n\pi_n). \tag{5}$$

The nth term in Eqs. (4) and (5) corresponds to a ray passing the sphere with a distance from the center of the particle of

$$d = (n + 1/2)\lambda/2\pi, \tag{6}$$

where λ is the incident wavelength. The terms with orders of $n + 1/2 \geq x$, where x is the size parameter (i.e., ray types in Fig. 6a,b) cannot be handled within the framework of the geometric optics method, but the

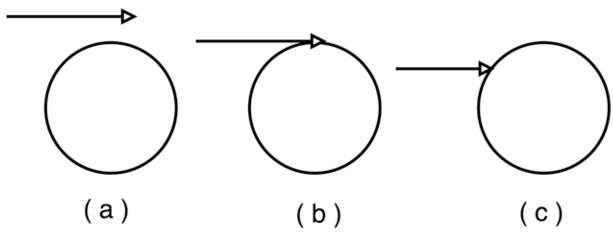

FIG. 6. Ray types: (a) edge rays, (b) grazing rays, and (c) rays incident on the particle.

contribution of lower-order rays (ray type in Fig. 6c) to the scattered radiation is taken into account. The contribution of ray types in Figs. 6a and b to the extinction efficiency is referred to as the edge effect and given as (Nussenzveig and Wiscombe 1980)

$$\Delta Q_{\mathrm{ext,edge\_effect}} = \frac{1.992\,386}{x^{2/3}}. \tag{7}$$

From Eq. (7), it is evident that the edge effect decreases with an increase in the size parameter. In the geometric optics regime, the contribution of the edge effect is virtually negligible. However, in the portion of the resonance regime where the particle size is on the order of the incident wavelength, it is critical to incorporate the contribution of the edge effect. In the case of the absorption efficiency, the edge effect is divided into above-/below-edge effect (Nussenzveig and Wiscombe 1980).

For nonspherical particles, analytical formulations of the edge effect and the above-/below-edge effect cannot be derived (Liou et al. 2011). To incorporate these effects into the present study, we postulate that the contributions of these effects to extinction and absorption efficiencies can be semiempirically formulated in the form

$$\Delta Q_{\mathrm{ext,edge\_effect}} = \frac{\eta_{\mathrm{ext}}}{(\pi D/\lambda)^{2/3}} \quad \text{and} \tag{8}$$

$$\Delta Q_{\mathrm{abs,edge\_effect}} = \frac{\eta_{\mathrm{abs}}}{(\pi D/\lambda)^{2/3}}, \tag{9}$$

where D is the maximum dimension of a nonspherical ice crystal and the parameters η_{ext} and η_{abs} are empirical coefficients. We compare the ADDA and IGOM solutions for the extinction and absorption efficiencies in the resonance regime to determine the empirical coefficients.

Unlike the conventional ray-tracing technique that assumes the extinction efficiency to have a constant value (i.e., $Q_{\mathrm{ext}} = 2$) regardless of the size parameter, the IGOM is able to mimic the variation of the extinction

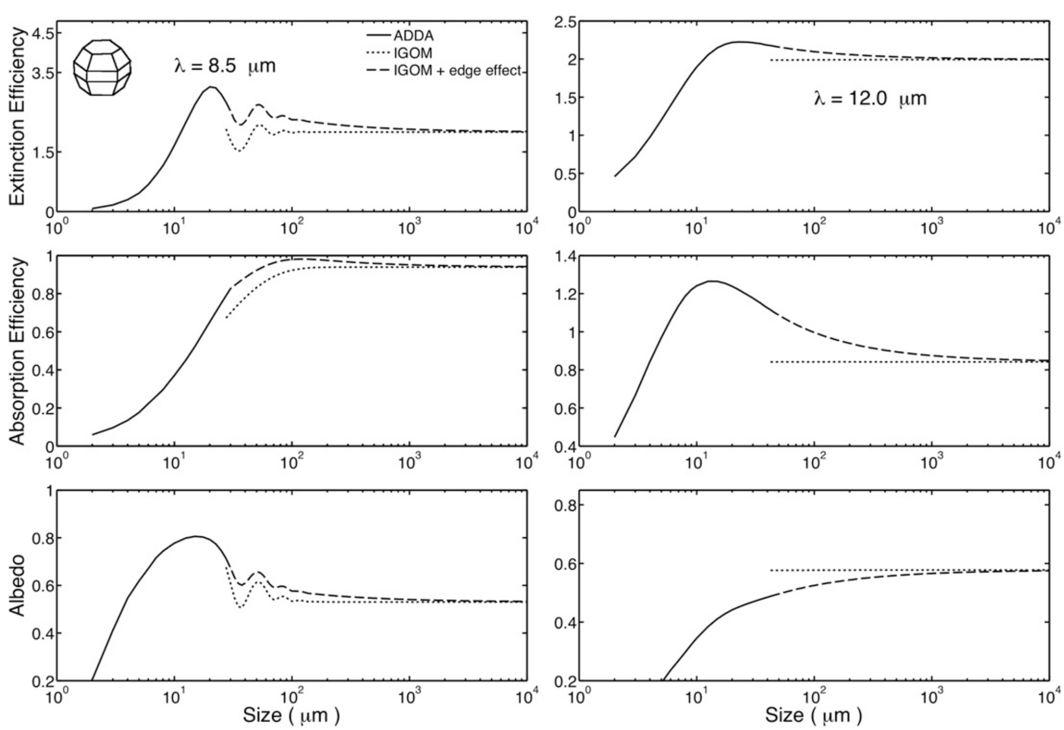

FIG. 7. Edge/tunneling effect contribution to the extinction efficiency, the absorption efficiency, and the single-scattering albedo.

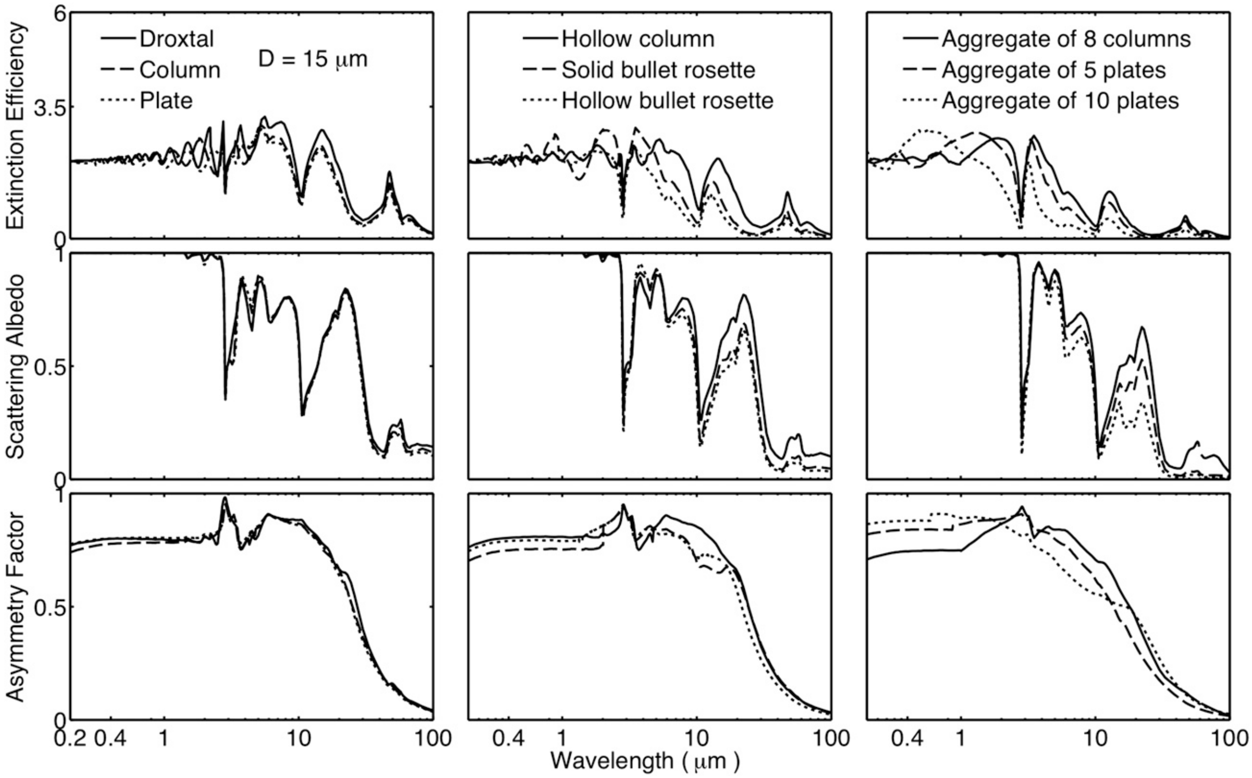

FIG. 8. Spectral variation of the extinction efficiency, the single-scattering albedo, and the asymmetry factor at the particle maximum dimension of 15 μm.

efficiency as a function of size parameter. However, the IGOM solution for Q_{ext} underestimates the particle's extinction because of the exclusion of the edge effect contribution, as illustrated by comparison between the ADDA and IGOM extinction efficiencies shown in Fig. 7. Note that the ADDA or FDTD are rigorous numerical methods fully accounting for the edge effect. The coefficient η_{ext} in Eq. (8) can be empirically determined such that the transition of the ADDA solution for Q_{ext} to the IGOM counterpart is continuous. A similar approach is applied to η_{abs} in Eq. (9). After the empirical addition of the edge effect to the IGOM results, the resulting extinction efficiency, indicated as the ''IGOM + edge effect'' in Fig. 7, is consistent with the ADDA results for moderate size parameters. The same approach is adopted to incorporate the above-/below-edge effect in the computation of the absorption efficiency. The efficiencies are used in the calculation of the single-scattering albedo, as shown in the bottom panels of Fig. 7.

3. Results

Based on the previous discussion, a data library was developed containing the single-scattering properties for a set of 11 ice habits. These properties were computed for 445 wavelengths and 189 particle sizes. The database includes the six nonzero phase matrix elements, extinction efficiency, asymmetry parameter, and single-scattering albedo. Additionally, the projected area and volume are provided for each given particle size. The phase matrix elements are computed at 498 scattering angles with an angular resolution of 0.01° from 0° to 2°, 0.05° from 2° to 5°, 0.1° from 5° to 10°, 0.5° from 10° to 15°, 1° from 15° to 176°, and 0.25° from 176° to 180°.

As an example, Fig. 8 shows the spectral variation of the integrated single-scattering properties (i.e., the extinction efficiency, single-scattering albedo, and asymmetry parameter) for nine ice crystal habits with a maximum diameter of 15 μm ($D_{\max} = 15$ μm). For the data shown in Fig. 8, the ice crystal surface is assumed to be smooth—that is, the parameter σ in Eq. (1) is assumed to be zero. Figure 9 is similar to Fig. 8, except for a larger size ($D_{\max} = 200$ μm). Figures 8 and 9 indicate that the extinction efficiency and single-scattering albedo are sensitive to ice crystal size.

To illustrate the integrated single-scattering properties as functions of both wavelength and particle size, Fig. 10 shows contours of these properties for a spatial

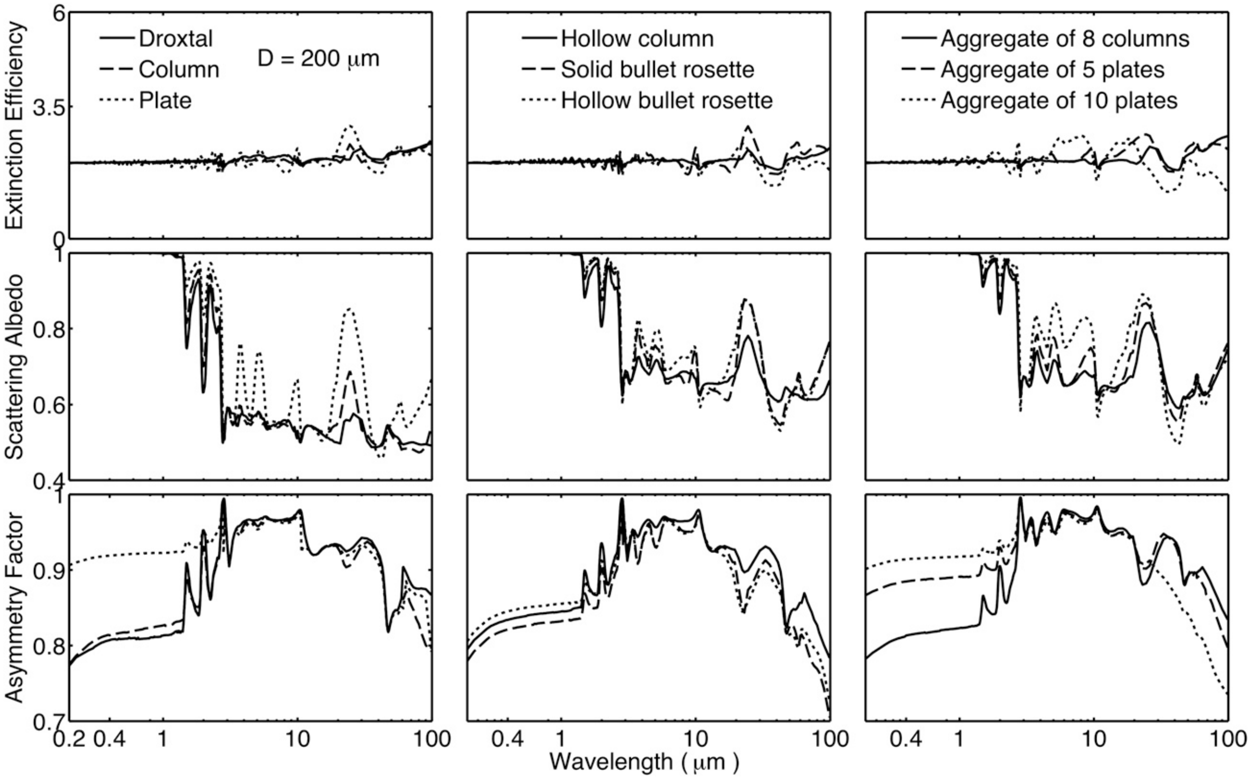

FIG. 9. As in Fig. 8, but for the particle maximum dimension of 200 μm.

aggregate of 10 plates (left column) and hollow bullet rosettes (right column) for wavelengths from 0.2 to 100 μm and particle sizes from 2 to 10 000 μm. In the asymmetry factor contours, the region marked in blue indicates the small size parameter regime, while the region marked in red indicates the geometric optics regime in which the asymmetry factor approaches its asymptotic value. The region marked in yellow indicates the resonance region in which the transition occurs from small to large size parameters; note that this region is quite narrow. The variation in the extinction efficiency is strongly correlated with the real part of the refractive index of ice shown in Fig. 1, whereas variation in the single-scattering albedo is sensitive to the imaginary part of the refractive index.

Figure 11 shows six elements of the phase matrix for the two habits in the previous figure—that is, the aggregate of 10 plates and the hollow bullet rosette. The maximum dimension is 20 μm and the incident wavelength is 0.65 μm ($x \sim 97$). Figure 12 is similar to Fig. 11, except that the size is 2000 μm. Ice halos are evident in Fig. 12 for large particle sizes but are not present for the small sizes depicted in Fig. 11. However, if the conventional geometric optics method (e.g., Takano and Liou 1989) that does not consider the ray-spreading effect (Bi et al. 2009) is applied, halos exist for all particle sizes. The dependence of the phase matrix elements on ice crystal habit is also evident in Figs. 11 and 12.

In the data library, single-scattering properties are provided for three surface roughness conditions (smooth, $\sigma = 0$; moderate roughness, $\sigma = 0.03$; severe roughness, $\sigma = 0.5$). Baum et al. (2010) discuss the impact of roughness and ice habit on the phase matrix. Further results are shown here, and Fig. 13 shows the phase function and the asymmetry factor for both smooth and roughened ice crystals. The scattering phase function corresponding to severe roughening is essentially featureless since the scattering becomes more random, and this effect of the surface roughness on the phase function has been confirmed experimentally (Barkey et al. 1999; Ulanowski et al. 2006). The asymmetry factor for roughened crystals is lower than their smooth crystal counterparts. A featureless phase function can be obtained numerically in several ways; for example, an inclusion of air bubbles or other inhomogeneities in ice crystals provides some possibilities (e.g., Macke et al. 1996a; C.-Labonnote et al. 2001).

For practical applications to remote sensing, the featureless phase function associated with roughened ice crystals yields quite different ice cloud property retrievals in comparison with smooth ice crystal retrieval results (Yang et al. 2008b; Zhang et al. 2009). Although

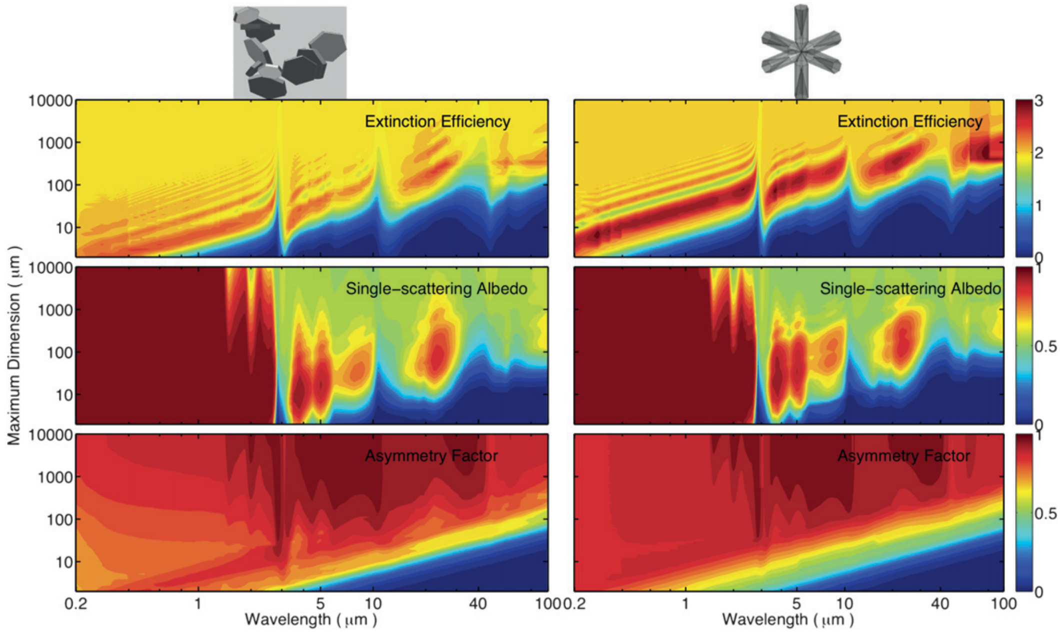

FIG. 10. Contours of the extinction efficiency, the single-scattering albedo, and the asymmetry factor for an aggregate of (left) 10 plates and (right) a hollow bullet rosette.

the detailed nature of ice crystal surface roughness is not known from a direct observational perspective, the existence of substantial ice crystal surface roughness or inhomogeneity has been suggested based on indirect evidence. While the exact mechanism causing the randomization of the scattering pattern is unknown, the resulting featureless phase function and associated single-scattering properties can be tested using polarized reflectance measurements following C.-Labonnote et al. (2001), Baran and C.-Labonnote (2007), and Cole et al.

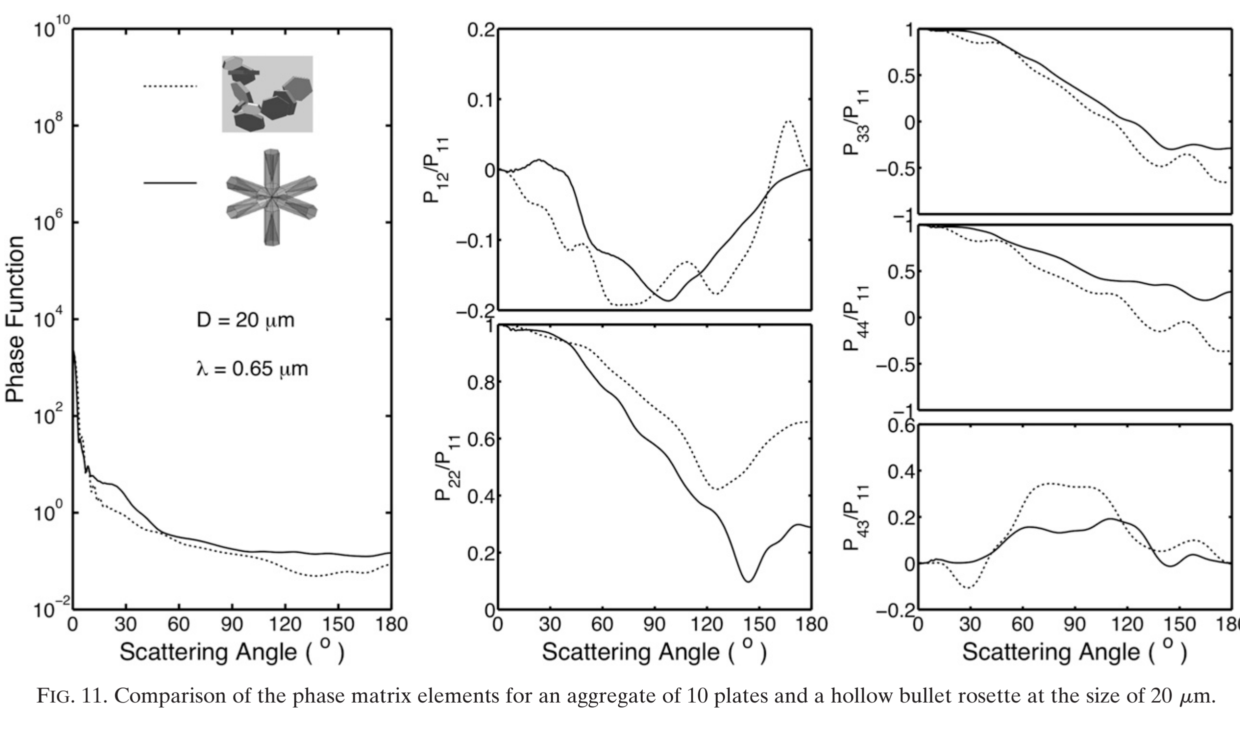

FIG. 11. Comparison of the phase matrix elements for an aggregate of 10 plates and a hollow bullet rosette at the size of 20 μm.

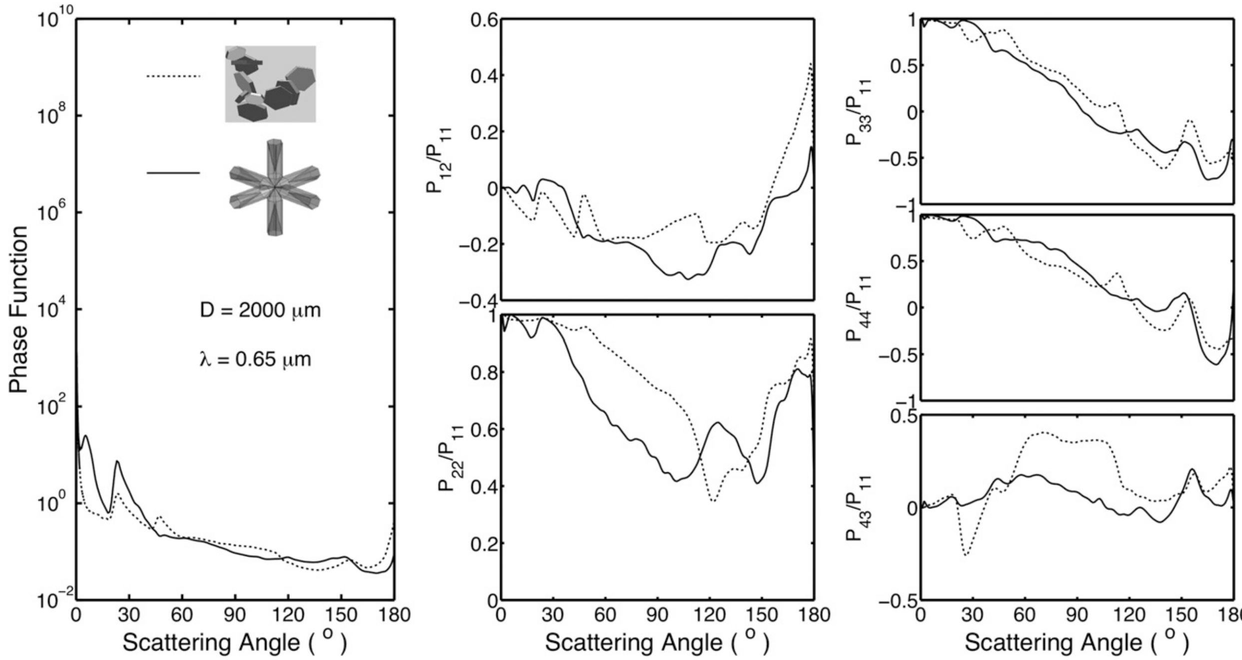

FIG. 12. As in Fig. 11, but for the size of 2000 μm.

(2013). Here, we use the ice cloud polarization reflectances measured by *Polarization and Anisotropy of Reflectances for Atmospheric Sciences Coupled with Observations from a Lidar* (*PARASOL*) to illustrate a consistency test of the smooth versus roughened ice bulk-scattering properties. The top panel of Fig. 14 shows the habit mixture used in the MODIS Collection 5 ice model (Baum et al. 2005). The middle and bottom panels of Fig. 14 show the bulk phase function P_{11} and the phase matrix element ratio $-P_{12}/P_{11}$ for smooth and severely rough ($\sigma = 0.5$) conditions for an effective particle size of 50 μm based on the ice crystal habit distribution shown in the top panel. Similar to the case for individual ice crystals, the bulk optical properties for an ensemble of ice crystals are strongly dependent on particle surface texture.

To test the effect of surface roughness on an ice model, simulations of polarized reflectance may be compared with data from *PARASOL*. The polarized reflectance is defined as (C.-Labonnote et al. 2001)

$$L_{\text{nmp}} = \frac{\pi\left(\pm\sqrt{Q^2 + U^2}\right)}{E_s}\frac{\cos\theta_s + \cos\theta_v}{\cos\theta_s}, \qquad (10)$$

where Q and U are the second and third Stokes parameters measured by *PARASOL*, E_s is solar irradiance at the top of the atmosphere, θ_s is the solar zenith angle, and θ_v is the viewing zenith angle. In Eq. (10), the sign is determined by the angle between the polarization vector and the normal to the scattering plane and the method is explained in detail by C.-Labonnote et al. (2001). To simulate the *PARASOL* polarized reflectance, we use the adding–doubling radiative transfer code for polarized radiative transfer developed by de Haan et al. (1987).

The top panel of Fig. 15 shows the density contours of polarized reflectance measurements at 865 nm from the *PARASOL* satellite on 15 October 2007. Over 60 000 ice cloudy pixels over the ocean are included, corresponding to approximately 866 000 total viewing geometries (note that for a given pixel, the *PARASOL* observations can provide up to 16 viewing angles). Only the cloudy pixels over the ocean that are determined to be ice phase and with 100% cloud cover are selected (Buriez et al. 1997). Baran and C.-Labonnote (2006) suggested that the peak near scattering angle 142° may be attributed to the influence of water clouds beneath optically thin ice clouds. In the case of a thin ice cloud above a water cloud, the *PARASOL* cloud mask algorithm may identify the pixel as ice phase although the effect of the underlying water cloud on the observed polarized reflectance is not negligible (Baran and C.-Labonnote 2006). The middle panel of Fig. 15 shows the differences between the theoretical simulations and observations (i.e., simulations minus observations) assuming smooth ice crystal models. The bottom panel of Fig. 15 is similar to the middle panel, except the bottom panel shows results assuming severely

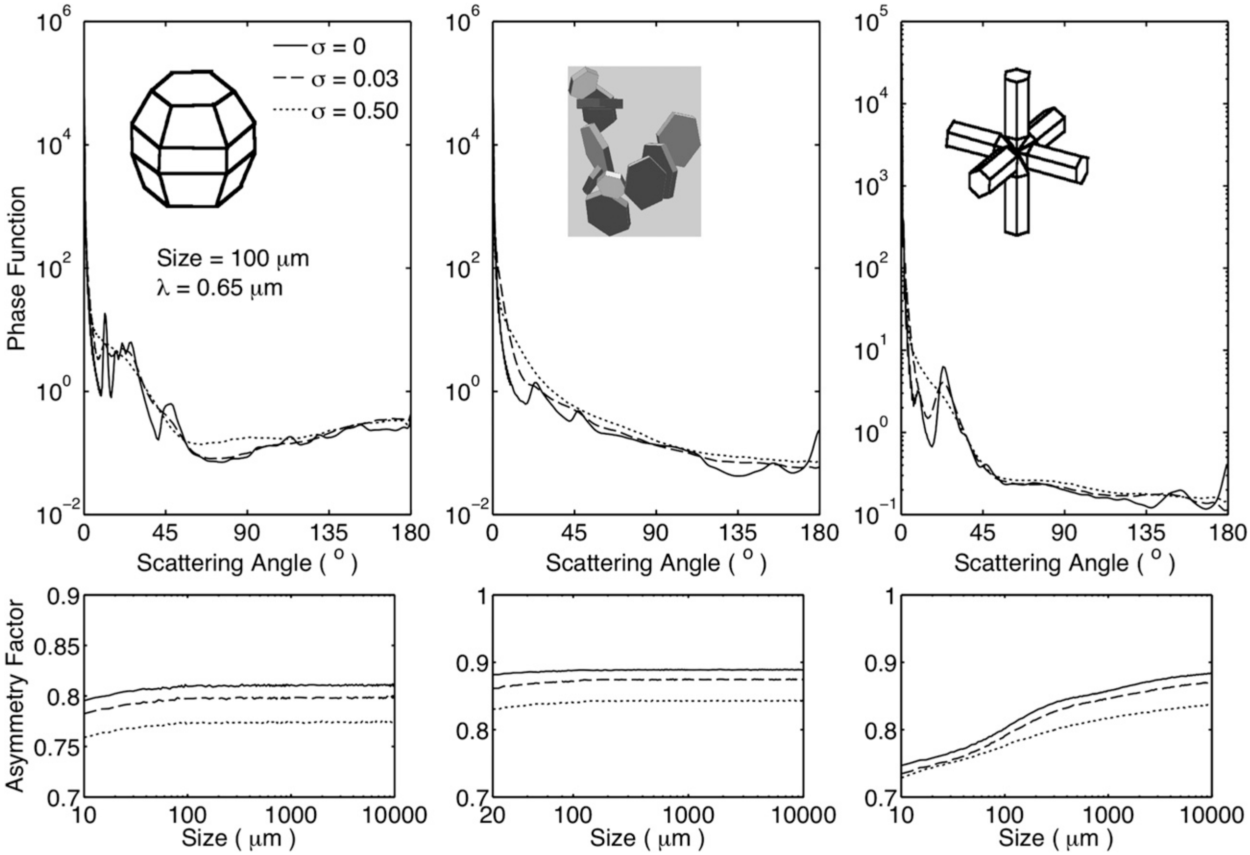

FIG. 13. Comparison of the phase function and the asymmetry factor for smooth (solid lines) and roughened (dashed lines) ice crystals.

roughened ice crystals. An optimal model should minimize the differences between simulations and observations, thereby leading to the most consistent results. From the comparison between the middle and bottom panels, it is clear that the roughened ice crystal model outperforms its smooth counterpart. These results support the conclusion by Zhang et al. (2009) that featureless phase functions should be used for operational satellite data processing.

4. Summary

This study discusses the development of a library containing the scattering, absorption, and polarization properties of ice particles in the spectral range from 0.2 to 100 μm. The properties are based on a combination of the Amsterdam discrete dipole approximation (ADDA), the T-matrix method, and the improved geometric optics method (IGOM). The electromagnetic edge effect is incorporated into the extinction and absorption efficiencies computed from the IGOM. A full set of single-scattering properties is provided by considering three-dimensional random orientations for 11 ice crystal habits: droxtals, prolate spheroids, oblate spheroids, solid and hollow columns, compact aggregates composed of 8 solid columns, hexagonal plates, small spatial aggregates composed of 5 plates, large spatial aggregates composed of 10 plates, and solid and hollow bullet rosettes. The maximum dimension for each habit ranges from 2 to 10 000 μm at 189 discrete sizes. For each ice habit, three roughness conditions (i.e., smooth, moderately roughened, and severely roughened surfaces) are considered to account for the surface texture for particles having relatively large size parameters. The data library contains the extinction efficiency, single-scattering albedo, asymmetry parameter, six independent nonzero elements of the phase matrix (P_{11}, P_{12}, P_{22}, P_{33}, P_{43}, and P_{44}), particle projected area, and particle volume.

The accuracy of the single-scattering properties for ice particles is improved by taking into consideration each of the following research advancements:

- accuracy of the extinction and absorption efficiencies at moderate to large size parameters are improved by the use of an empirical approach to include the edge and the above-/below-edge effects on ice crystal optical properties;

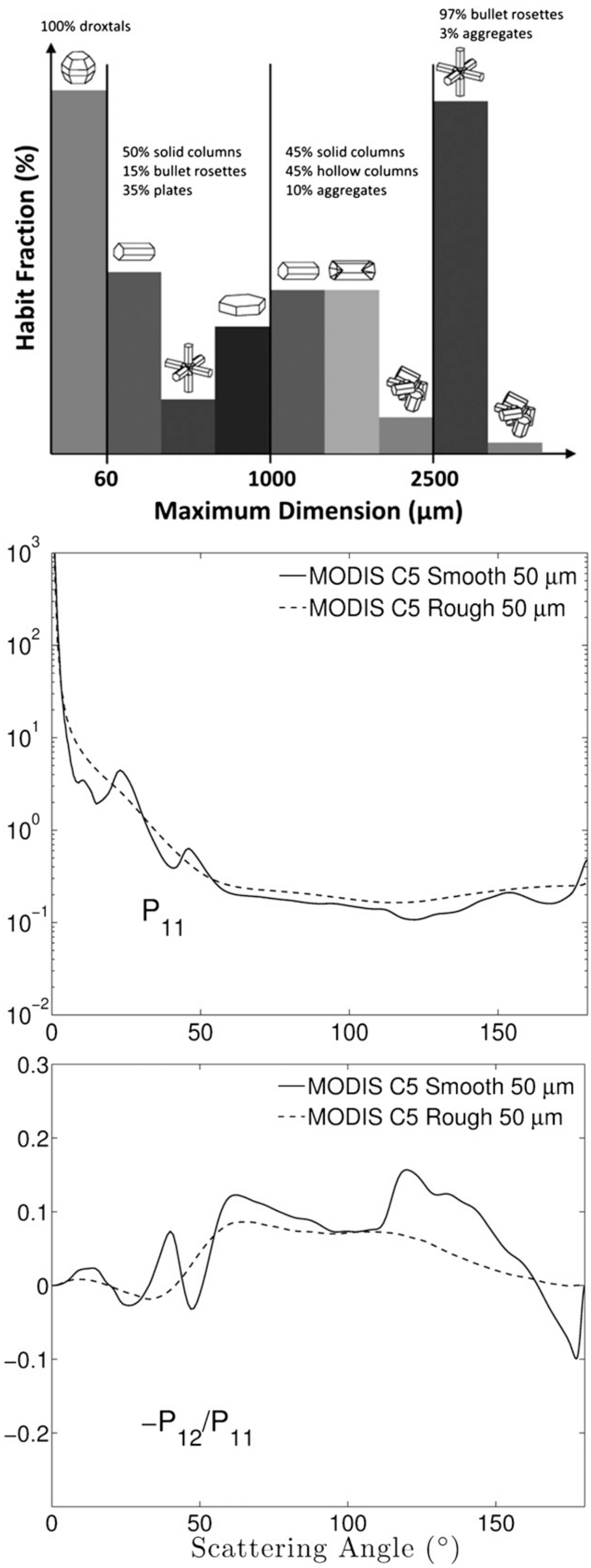

FIG. 14. (top) Ice crystal habit distribution assumed for MODIS Collection 5 ice cloud property retrieval. (middle) Comparison of ← the phase functions of smooth and roughened ice crystals with an effective particle size of 50 μm based on the habit distribution in (top), and (bottom) the phase matrix element ratio $-P_{12}/P_{11}$ corresponding to the phase functions in (middle).

- the single-scattering calculations use an updated compilation of the real and imaginary parts of the refractive index for ice given by Warren and Brandt (2008);
- the aspect ratio of each habit is consistent for all wavelengths;
- the phase matrix elements for randomly oriented ice crystals are provided in the database, enabling consideration of the transfer of polarized light beams involving ice clouds;
- a new treatment of forward scattering in the IGOM is implemented that renders obsolete the delta-transmission energy term; and
- the single-scattering properties are provided for new habits including the hollow bullet rosette and the small and large spatial aggregates of plates.

The size of the library is approximately 200 GB, and includes the single-scattering properties of ice crystals covering the wavelengths from UV to far IR. This data library is complementary to those presented by Kim (2006), Liu (2008), and Hong et al. (2009) for the microwave regime.

This library provides the basic single-scattering properties that are critical for ice cloud remote sensing applications and radiative transfer simulations. An illustration of the improved consistency was provided through a comparison of *PARASOL* polarized reflectance measurements with theoretical simulations. The resulting comparison between measurements and simulations clearly demonstrated that ice cloud optical models assuming severely roughened ice crystals significantly outperform their counterparts assuming smooth ice crystals.

Another point made in this study is that the assumption of severe roughening for the ice crystals results in decreasing the asymmetry parameter at solar wavelengths. The decrease of the asymmetry parameter, and use of the featureless phase function, at solar wavelengths implies a decrease in the inferred optical thickness for an ice cloud. This, in turn, will improve the consistency of ice cloud optical thickness inferred from solar and IR wavelengths.

A long-term goal of the authors has been to provide ice crystal single-scattering properties that lead to more consistent retrievals from sensors taking measurements at solar to far-infrared wavelengths, including polarization

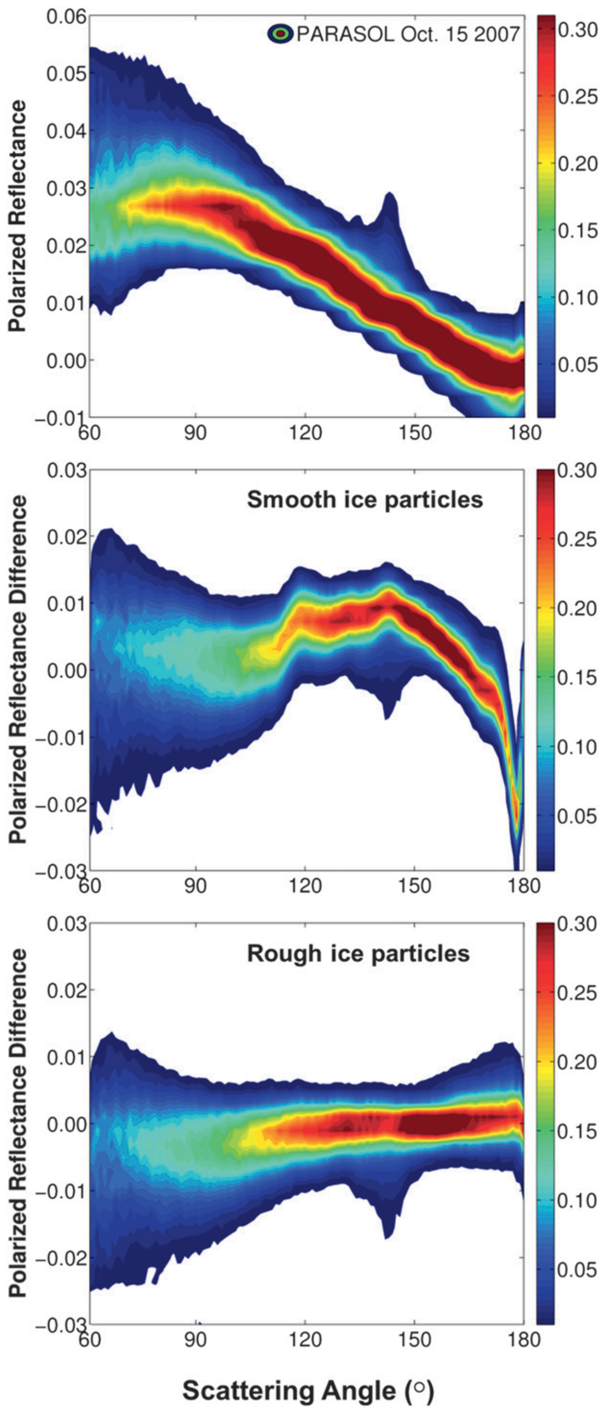

FIG. 15. (top) Density contours of polarized reflectance measurements at 865 nm from the *PARASOL* satellite on 15 Oct 2007. Over 60 000 pixels over the ocean are included, corresponding to approximately 866 000 total viewing geometries plotted. (middle) The difference between simulated polarized reflectance and measured polarized reflectance for each viewing geometry. The MODIS Collection 5 habit distribution and smooth ice particles with an effective diameter of 50 μm were used in the simulation, and the optical depth was 5. (bottom) The difference in polarized reflectance using C5 with severely roughened ice particles and all simulation parameters the same as (middle).

measurements. This library could be a useful resource for the atmospheric radiative transfer and remote sensing research community.

Acknowledgments. The computation of the present scattering database was mainly supported by NASA Grant NNX11AK37G managed by Dr. Lucia Tsaoussi, and partly by the endowment funds related to the David Bullock Harris Chair in Geosciences at the College of Geosciences, Texas A&M University. The long-term effort on the further development and refinement of the Improved Geometric Optics Model (IGOM) was mainly supported by the National Science Foundation (Grants ATM-0239605 and ATM-0803779). Bryan Baum and Ping Yang also gratefully acknowledge the support of Grant NNX11AR06G managed by Dr. Hal Maring and Grant NNX11AF40G managed by Dr. Ramesh Kakar. George W. Kattawar's research was supported by the Office of Naval Research under Contract N00014-11-1-0154. Michael Mishchenko's research was funded by the NASA Remote Sensing Theory Program managed by Dr. Lucia Tsaoussi and the NASA Radiation Sciences Program managed by Dr. Hal Maring. The authors thank M. A. Yurkin and A. G. Hoekstra for the use of their ADDA code (version 0.79), J. F. de Haan for the adding–doubling code for the transfer of polarized radiation, and Y. Xie for the definition of spatial aggregates of hexagonal plates.

REFERENCES

Arnott, W. P., Y. Dong, J. Hallett, and M. R. Poellot, 1994: Role of small ice crystals in radiative properties of cirrus: A case study, FIRE II, November 22, 1991. *J. Geophys. Res.,* **99** (D1), 1371–1381.

Auer, A. H., Jr., and D. L. Veal, 1970: The dimension of ice crystals in natural clouds. *J. Atmos. Sci.,* **27,** 919–926.

Baran, A. J., 2009: A review of the light scattering properties of cirrus. *J. Quant. Spectrosc. Radiat. Transfer,* **110,** 1239–1260.

——, and S. Havemann, 1999: Rapid computation of the optical properties of hexagonal columns using complex angular momentum theory. *J. Quant. Spectrosc. Radiat. Transfer,* **63,** 499–519.

——, and P. N. Francis, 2004: On the radiative properties of cirrus cloud at solar and thermal wavelengths: A test of model consistency using high-resolution airborne radiance measurements. *Quart. J. Roy. Meteor. Soc.,* **130,** 763–778.

——, and L. C.-Labonnote, 2006: On the reflection and polarization properties of ice cloud. *J. Quant. Spectrosc. Radiat. Transfer,* **100,** 41–54.

——, and ——, 2007: A self-consistent scattering model for cirrus. I: The solar region. *Quart. J. Roy. Meteor. Soc.,* **133,** 1899–1912.

——, P. Yang, and S. Havemann, 2001: Calculation of the single-scattering properties of randomly oriented hexagonal ice columns: A comparison of the T-matrix and the finite-difference time-domain methods. *Appl. Opt.,* **40,** 4376–4386.

Barkey, B., K. N. Liou, Y. Takano, W. Gellerman, and P. Sokolsky, 1999: An analog light scattering experiment of hexagonal icelike particles. Part II: Experimental and theoretical results. *J. Atmos. Sci.,* **56,** 613–625.

Baum, B. A., P. Yang, A. J. Heymsfield, S. Platnick, M. D. King, and S. T. Bedka, 2005: Bulk scattering models for the remote sensing of ice clouds. Part II: Narrowband models. *J. Appl. Meteor.,* **44,** 1896–1911.

——, ——, Y.-X. Hu, and Q. Feng, 2010: The impact of ice particle roughness on the scattering phase matrix. *J. Quant. Spectrosc. Radiat. Transfer,* **111,** 2534–2549, doi:10.1016/j.jqsrt.2010.07.008.

——, ——, A. J. Heymsfield, C. G. Schmitt, Y. Xie, A. Bansemer, Y.-X. Hu, and Z. Zhang, 2011: Improvements in shortwave bulk scattering and absorption models for the remote sensing of ice clouds. *J. Appl. Meteor. Climatol.,* **50,** 1037–1056.

Bi, L., P. Yang, G. W. Kattawar, and R. Kahn, 2008: Single-scattering properties of tri-axial ellipsoidal particles for a size parameter range from the Rayleigh to geometric-optics regimes. *Appl. Opt.,* **48,** 114–126.

——, ——, ——, B. A. Baum, Y. X. Hu, D. M. Winker, R. S. Brock, and J. Q. Lu, 2009: Simulation of the color ratio associated with the backscattering of radiation by ice particles at the wavelengths of 0.532 and 1.064 μm. *J. Geophys. Res.,* **114,** D00H08, doi:10.1029/2009JD011759.

——, ——, ——, Y. Hu, and B. A. Baum, 2011a: Diffraction and external reflection by dielectric faceted particles. *J. Quant. Spectrosc. Radiat. Transfer,* **112,** 163–173.

——, ——, ——, ——, and ——, 2011b: Scattering and absorption of light by ice particles: Solution by a new physical-geometric optics hybrid method. *J. Quant. Spectrosc. Radiat. Transfer,* **112,** 1492–1508.

Bohren, C. F., and D. R. Huffman, 1983: *Absorption and Scattering of Light by Small Particles.* John Wiley and Sons, 530 pp.

Borovoi, A., I. Grishin, E. Naats, and U. Oppel, 2002: Light backscattering by hexagonal ice crystals. *J. Quant. Spectrosc. Radiat. Transfer,* **72,** 403–417.

Buriez, J.-C., C. Vanbauce, F. Parol, P. Goloub, M. Herman, B. Bonnel, Y. Fouquart, P. Couvert, and G. Seze, 1997: Cloud detection and derivation of cloud properties from POLDER. *Int. J. Remote Sens.,* **18,** 2785–2813.

Cai, Q. M., and K. N. Liou, 1982: Theory of polarized light scattering by hexagonal ice crystals. *Appl. Opt.,* **21,** 3569–3580.

C.-Labonnote, L., G. Brogniez, J.-C. Buriez, M. Doutriaux-Boucher, J.-F. Gayet, and A. Macke, 2001: Polarized light scattering by inhomogeneous hexagonal monocrystals: Validation with ADEOS-POLDER measurements. *J. Geophys. Res.,* **106** (D11), 12 139–153.

Cole, B. H., P. Yang, B. A. Baum, J. Riedi, L. C.-Labonnote, F. Thieuleux, and S. Platnick, 2013: Comparison of *PARASOL* observations with polarized reflectances simulated using different ice habit mixtures. *J. Appl. Meteor. Climatol.,* in press.

Connolly, P. J., M. J. Flynn, Z. Ulanowski, T. W. Choularton, M. W. Gallagher, and K. N. Bower, 2007: Calibration of cloud particle imager probes using calibration beads and ice crystal analogs: The depth of field. *J. Atmos. Oceanic Technol.,* **24,** 1860–1879.

Cox, S. C., and W. H. Munk, 1954: Measurement of the roughness of the sea surface from photographs of the sun's glitter. *J. Opt. Soc. Amer.,* **44,** 838–850.

Davis, P. J., and P. Rabinowitz, 1975: *Methods of Numerical Integration.* Academic Press, 459 pp.

de Haan, J. F., P. B. Bosma, and J. W. Hovenier, 1987: The adding method for multiple scattering calculations of polarized light. *Astron. Astrophys.,* **183,** 371–391.

Edwards, J. M., S. Havemann, J. C. Thelen, and A. J. Baran, 2007: A new parameterization for the radiative properties of ice crystals: Comparison with existing schemes and impact in a GCM. *Atmos. Res.,* **83,** 19–34.

Fu, Q., P. Yang, and W. B. Sun, 1998: An accurate parameterization of the infrared radiative properties of cirrus clouds for climate models. *J. Climate,* **11,** 2223–2237.

Gu, Y., J. Farrara, K. N. Liou, and C. R. Mechoso, 2003: Parameterization of cloud-radiation processes in the UCLA general circulation model. *J. Climate,* **16,** 3357–3370.

Ham, S.-H., B.-J. Sohn, P. Yang, and B. A. Baum, 2009: Assessment of the quality of MODIS cloud products from radiance simulations. *J. Appl. Meteor. Climatol.,* **48,** 1591–1612.

Havemann, S., and A. J. Baran, 2001: Extension of T-matrix to scattering of electromagnetic plane waves by non-axisymmetric dielectric particles: Application to hexagonal ice cylinders. *J. Quant. Spectrosc. Radiat. Transfer,* **70,** 139–158.

Hess, M., and M. Wiegner, 1994: COP: A data library of optical properties of hexagonal ice crystals. *Appl. Opt.,* **33,** 7740–7746.

——, P. Koepke, and I. Schult, 1998: Optical properties of aerosols and clouds: The software package OPAC. *Bull. Amer. Meteor. Soc.,* **79,** 831–844.

Hesse, E., and Z. Ulanowski, 2003: Scattering from long prisms computed using ray tracing combined with diffraction on facets. *J. Quant. Spectrosc. Radiat. Transfer,* **79–80,** 721–732.

Hong, G., P. Yang, B. A. Baum, A. J. Heymsfield, F. Weng, Q. Liu, G. Heygster, and S. A. Buehler, 2009: Scattering database in the millimeter and submillimeter wave range of 100–1000 GHz for nonspherical ice particles. *J. Geophys. Res.,* **114,** D06201, doi:10.1029/2008JD010451.

Huang, H.-L., P. Yang, H. Wei, B. A. Baum, Y. X. Hu, P. Atonelli, and S. A. Ackerman, 2004: Inference of ice cloud properties from high-spectral resolution infrared observations. *IEEE Trans. Geosci. Remote Sens.,* **42,** 842–853.

Iwabuchi, H., P. Yang, K. N. Liou, and P. Minnis, 2012: Physical and optical properties of persistent contrails: Climatology and interpretation. *J. Geophys. Res.,* **117,** D06215, doi:10.1029/2011JD017020.

Kahnert, F. M., 2003: Numerical methods in electromagnetic scattering theory. *J. Quant. Spectrosc. Radiat. Transfer,* **79–80,** 775–824.

Key, J. R., P. Yang, B. A. Baum, and S. L. Nasiri, 2002: Parameterization of shortwave ice cloud optical properties for various particle habits. *J. Geophys. Res.,* **107,** 4181, doi:10.1029/2001JD000742.

Kim, M.-J., 2006: Single scattering parameters of randomly oriented snow particles at microwave frequencies. *J. Geophys. Res.,* **111,** D14201, doi:10.1029/2005JD006892.

King, M. D., S. Platnick, P. Yang, G. T. Arnold, M. A. Gray, J. C. Riedi, S. A. Ackerman, and K. N. Liou, 2004: Remote sensing of liquid water and ice cloud optical thickness, and effective radius in the Arctic: Application of airborne multispectral MAS data. *J. Atmos. Oceanic Technol.,* **21,** 857–875.

Liou, K. N., 1986: Influence of cirrus clouds on weather and climate processes: A global perspective. *Mon. Wea. Rev.,* **114,** 1167–1199.

——, 2002: *An Introduction to Atmospheric Radiation.* 2nd ed. International Geophysical Series, Vol. 84, Academic Press, 583 pp.

——, Y. Gu, Q. Yue, and G. McFarguhar, 2008: On the correlation between ice water content and ice crystal size and its application to radiative transfer and general circulation models. *Geophys. Res. Lett.,* **35,** L13805, doi:10.1029/2008GL033918.

——, Y. Takano, and P. Yang, 2010: On geometric optics and surface waves for light scattering by spheres. *J. Quant. Spectrosc. Radiat. Transfer,* **111,** 1980–1989, doi:10.1016/j.jqsrt.2010.04.004.

——, ——, and ——, 2011: Light absorption and scattering by aggregates: Application to black carbon and snow grain. *J. Quant. Spectrosc. Radiat. Transfer,* **112,** 1581–1594, doi:10.1016/j.jqsrt.2011.03.007.

Liu, G., 2008: A database of microwave single-scattering properties for nonspherical ice particles. *Bull. Amer. Meteor. Soc.,* **89,** 1563–1570.

Lynch, D. K., K. Sassen, D. O. Starr, and G. Stephens, 2002: *Cirrus.* Oxford University Press, 480 pp.

Macke, A., 1993: Scattering of light by polyhedral ice crystals. *Appl. Opt.,* **32,** 2780–2788.

——, M. I. Mishchenko, and B. Cains, 1996a: The influence of inclusions on light scattering by large ice particles. *J. Geophys. Res.,* **101** (D18), 23 311–23 316.

——, J. Mueller, and E. Raschke, 1996b: Single scattering properties of atmospheric ice crystal. *J. Atmos. Sci.,* **53,** 2813–2825.

Mayer, B., and A. Kylling, 2005: Technical note: The libRadtran software package for radiative transfer calculations—Description and examples of use. *Atmos. Chem. Phys.,* **5,** 1855–1877.

McFarquhar, G. M., P. Yang, A. Macke, and A. J. Baran, 2002: A new parameterization of single-scattering solar radiative properties for tropical anvils using observed ice crystal size and shape distributions. *J. Atmos. Sci.,* **59,** 2458–2478.

Minnis, P., and Coauthors, 2011: CERES Edition-2 cloud property retrievals using TRMM VIRS and TERRA and AQUA MODIS data—Part I: Algorithms. *IEEE Trans. Geosci. Remote Sens.,* **49,** 4374–4400.

Mishchenko, M. I., and A. Macke, 1998: Incorporation of physical optics effects and computations of the Legendre expansion for ray-tracing phase functions involving delta-function transmission. *J. Geophys. Res.,* **103** (D2), 1799–1805.

——, and K. Sassen, 1998: Depolarization of lidar returns by small ice crystals: An application to contrails. *Geophys. Res. Lett.,* **25,** 309–312.

——, L. D. Travis, and D. W. Mackowski, 1996: T-matrix computations of light scattering by nonspherical particles: A review. *J. Quant. Spectrosc. Radiat. Transfer,* **55,** 535–575.

——, W. J. Wiscombe, J. W. Hovenier, and L. D. Travis, 2000: Overview of scattering by nonspherical particles. *Light Scattering by Nonspherical Particles: Theory, Measurements, and Geophysical Applications,* M. I. Mishchenko, J. W. Hovenier, and L. D. Travis, Eds., Academic Press, 29–60.

——, L. D. Travis, and A. A. Lacis, 2002: *Scattering, Absorption, and Emission of Light by Small Particles.* Cambridge University Press, 462 pp.

Mitchell, D. L., and W. P. Arnott, 1994: A model predicting the evolution of ice particle size spectra and radiative properties of cirrus clouds. Part II: Dependence of absorption and extinction on ice crystal morphology. *J. Atmos. Sci.,* **51,** 817–832.

Muinonen, K., 1989: Scattering of light by crystals: A modified Kirchhoff approximation. *Appl. Opt.,* **28,** 3044–3050.

Nakajima, T. Y., T. Nakajima, K. Yoshimori, S. K. Mishra, and S. N. Tripathi, 2009: Development of a light scattering solver applicable to particles of arbitrary shape on the basis of the surface-integral equations method of Müller type. I. Methodology, accuracy of calculation, and electromagnetic current on the particle surface. *Appl. Opt.,* **48,** 3526–3536.

Nussenzveig, H. M., and W. J. Wiscombe, 1980: Efficiency factors in Mie scattering. *Phys. Rev. Lett.,* **18,** 1490–1494.

Platnick, S., M. D. King, S. A. Ackerman, W. P. Menzel, B. A. Baum, J. C. Riedi, and R. A. Frey, 2003: The MODIS cloud products: Algorithms and examples from Terra. *IEEE Trans. Geosci. Remote Sens.,* **41,** 459–473.

Pruppacher, H. R., and J. D. Klett, 1980: *Microphysics of Clouds and Precipitation.* Springer, 714 pp.

Schmitt, C. G., and A. J. Heymsfield, 2007: On the occurrence of hollow bullet rosette– and column-shaped ice crystals in midlatitude cirrus. *J. Atmos. Sci.,* **64,** 4515–4520.

Sun, W., Q. Fu, and Z. Chen, 1999: Finite-difference time-domain solution of light scattering by dielectric particles with perfectly matched layer absorbing boundary conditions. *Appl. Opt.,* **38,** 3141–3151.

Takano, Y., and K. N. Liou, 1989: Solar radiative transfer in cirrus clouds. Part I. Single-scattering and optical properties of hexagonal ice crystals. *J. Atmos. Sci.,* **46,** 3–19.

——, and ——, 1995: Radiative transfer in cirrus clouds. Part III: Light scattering by irregular ice crystals. *J. Atmos. Sci.,* **52,** 818–837.

Ulanowski, Z., E. Hesse, P. H. Kaye, and A. J. Baran, 2006: Light scattering by complex ice-analogue crystals. *J. Quant. Spectrosc. Radiat. Transfer,* **100,** 382–392.

Um, J. S., and G. M. McFarquhar, 2007: Single-scattering properties of aggregates of bullet rosettes in cirrus. *J. Appl. Meteor. Climatol.,* **46,** 757–775.

van de Hulst, H. C., 1957: *Light Scattering by Small Particles.* Dover, 470 pp.

Walden, V. P., S. G. Warren, and E. Tuttle, 2003: Atmospheric ice crystals over the Antarctic Plateau in winter. *J. Appl. Meteor.,* **42,** 1391–1405.

Wang, X., K. N. Liou, S. C. Ou, G. G. Mace, and M. Deng, 2009: Remote sensing of cirrus cloud vertical size profile using MODIS data. *J. Geophys. Res.,* **114,** D09205, doi:10.1029/2008JD011327.

Warren, S. G., and R. E. Brandt, 2008: Optical constants of ice from the ultraviolet to the microwave: A revised compilation. *J. Geophys. Res.,* **113,** D14220, doi:10.1029/2007JD009744.

Wendisch, M., P. Yang, and P. Pilewskie, 2007: Effects of ice crystal habit on the thermal infrared radiative properties and forcing of cirrus clouds. *J. Geophys. Res.,* **112,** D08201, doi:10.1029/2006JD007899.

Wendling, P., R. Wendling, and H. K. Weickmann, 1979: Scattering of solar radiation by hexagonal ice crystals. *Appl. Opt.,* **18,** 2663–2671.

Wriedt, T., 2009: Light scattering theories and computer codes. *J. Quant. Spectrosc. Radiat. Transfer,* **110,** 833–843.

Xie, Y., P. Yang, G. W. Kattawar, B. A. Baum, and Y. Hu, 2011: Simulation of the optical properties of plate aggregates for application to the remote sensing of cirrus clouds. *Appl. Opt.,* **50,** 1065–1081.

Yang, P., and K. N. Liou, 1996a: Finite-difference time domain method for light scattering by small ice crystals in three-dimensional space. *J. Opt. Soc. Amer.,* **13A,** 2072–2085.

——, and ——, 1996b: Geometric-optics-integral-equation method for light scattering by nonspherical ice crystals. *Appl. Opt.,* **35,** 6568–6584.

——, and ——, 1998: Single-scattering properties of complex ice crystals in terrestrial atmosphere. *Contrib. Atmos. Phys.,* **71,** 223–248.

——, and ——, 2009a: Effective refractive index for determining ray propagation in an absorbing dielectric particle. *J. Quant. Spectrosc. Radiat. Transfer,* **110,** 300–306.

——, and ——, 2009b: An ''exact'' geometric-optics approach for computing the optical properties of large absorbing particles. *J. Quant. Spectrosc. Radiat. Transfer,* **110,** 1162–1177.

——, ——, K. Wyser, and D. Mitchell, 2000: Parameterization of the scattering and absorption properties of individual ice crystals. *J. Geophys. Res.,* **105** (D4), 4699–4718.

——, B. A. Baum, A. J. Heymsfield, Y. X. Hu, H.-L. Huang, S.-C. Tsay, and S. Ackerman, 2003: Single-scattering properties of droxtals. *J. Quant. Spectrosc. Radiat. Transfer,* **79–80,** 1159–1169.

——, H. Wei, H.-L. Huang, B. A. Baum, Y. X. Hu, G. W. Kattawar, M. I. Mishchenko, and Q. Fu, 2005: Scattering and absorption property database for nonspherical ice particles in the near- through far-infrared spectral region. *Appl. Opt.,* **44,** 5512–5523.

——, and Coauthors, 2008a: Effect of cavities on the optical properties of bullet rosettes: Implications for active and passive remote sensing of ice cloud properties. *J. Appl. Meteor. Climatol.,* **47,** 2311–2330.

——, G. Hong, G. W. Kattawar, P. Minnis, and Y. Hu, 2008b: Uncertainties associated with the surface texture of ice particles in satellite-based retrieval of cirrus clouds: Part II—Effect of particle surface roughness on retrieved cloud optical thickness and effective particle size. *IEEE Trans. Geosci. Remote Sens.,* **46,** 1948–1957.

——, ——, A. E. Dessler, S. C. Ou, K. N. Liou, P. Minnis, and Hashvardhan, 2010: Contrails and induced cirrus: Optics and radiation. *Bull. Amer. Meteor. Soc.,* **91,** 473–478.

Yee, S. K., 1966: Numerical solution of initial boundary value problems involving Maxwell's equations in isotropic media. *IEEE Trans. Antennas Propag.,* **14,** 302–307.

Yue, Q., K. N. Liou, S. C. Ou, B. H. Kahn, P. Yang, and G. G. Mace, 2007: Interpretation of AIRS data in thin cirrus atmospheres based on a fast radiative transfer model. *J. Atmos. Sci.,* **64,** 3827–3842.

Yurkin, M. A., A. G. Hoekstra, R. Scott Brock, and J. Q. Lu, 2007a: Systematic comparison of the discrete dipole approximation and the finite difference time domain method for large dielectric scatterers. *Opt. Express,* **15,** 17 902–17 911.

——, V. P. Maltsev, and A. G. Hoekstra, 2007b: The discrete dipole approximation for simulation of light scattering by particles much larger than the wavelength. *J. Quant. Spectrosc. Radiat. Transfer,* **106,** 546–557.

Zhang, Z., and Coauthors, 2004: Geometric optics solution to light scattering by droxtal ice crystals. *Appl. Opt.,* **43,** 2490–2499.

——, P. Yang, G. W. Kattawar, J. Riedi, L. C.-Labonnote, B. A. Baum, S. Platnick, and H.-L. Huang, 2009: Influence of ice particle model on retrieving cloud optical thickness from satellite measurements: model comparison and implication for climate study. *Atmos. Chem. Phys.,* **9,** 7115–7129.